Energy Advances

ROYAL SOCIETY OF CHEMISTRY

COMMUNICATION

View Article Online
View Journal | View Issue

Check for updates

Cite this: *Energy Adv.*, 2025, 4, 1006

Received 23rd April 2025,
Accepted 12th June 2025

DOI: 10.1039/d5ya00112a

rsc.li/energy-advances

In situ confinement of ultrahigh-density Co_2P nanoparticles within biomass-derived carbon nanosheet frameworks as efficient cocatalysts for solar H_2 production†

Fang Wang,[ab] Junqing Wang,[ab] Jiao Zhang,[c] Yiming Li,[c] Zhengguo Zhang[ab] and Shixiong Min *[abc]

In this work, an efficient and cost-effective H_2 evolution cocatalyst (Co_2P/CPE) is developed by *in situ* confinement of ultrahigh-density Co_2P nanoparticles within a carbonized *Pleurotus eryngii* (CPE) matrix. Benefiting from the ultrathin carbon nanosheet architectures and exposure of ultradense Co_2P nanoparticles (NPs), Co_2P/CPE exhibits superior cocatalytic performance for the photocatalytic H_2 evolution reaction (HER) in an Erythrosin B-triethanolamine (ErB-TEOA) system under visible light ($\lambda \geq 420$ nm), achieving an exceptionally high H_2 evolution rate of 449 µmol h^{-1} with an apparent quantum efficiency (AQE) of 8.7% at 500 nm. Remarkably, the excellent structural integrity ensures outstanding stability during consecutive HER cycles over 36 h. Furthermore, Co_2P/CPE demonstrates excellent versatility as an active and durable cocatalyst to significantly enhance the photocatalytic HER activity of CdS NPs under visible light ($\lambda \geq 420$ nm). This work establishes a paradigm for designing cost-effective and efficient HER cocatalysts through synergistic integration of biomass-derived carbon architectures with precisely engineered active sites.

The ever-increasing global energy demand coupled with escalating environmental challenges has necessitated urgent development of sustainable energy alternatives to finite fossil fuels.[1–3] Hydrogen (H_2), as a carbon-neutral energy carrier with exceptional gravimetric energy density (142 MJ kg^{-1}), has emerged as a cornerstone for future clean energy systems.[4–8] Among the H_2 production methods developed to date, solar-driven photocatalytic water splitting presents a promising solution by enabling the direct conversion of abundant solar energy into clean chemical energy stored in H_2.[9–12] Despite decades of efforts, practical implementation of the photocatalytic water splitting technology remains hindered by critical limitations in designing efficient photocatalytic systems/photocatalysts, primarily due to the rapid charge carrier recombination and sluggish surface reaction kinetics. While noble metal-based cocatalysts (*e.g.*, Pt, Ag, Au) can mitigate these limitations through effective charge separation and reduced activation energy for the HER, their high cost and scarcity fundamentally constrain scalable applications.[13–15] This paradox has driven intensive exploration of transition metal-based cocatalysts as viable and cost-effective alternatives.[16,17] Among them, transition metal phosphides (TMPs) have shown particular promise due to their optimal d-band electronic structure that balances H adsorption energetics and excellent electrical conductivity.[18–23] Specifically, cobalt phosphides (*e.g.*, Co_2P and CoP) displaying high activity and excellent durability have been extensively employed as cocatalysts in both dye-sensitized and semiconductor-based photocatalytic HER systems.[24–26] However, to achieving high activity while maintaining long-term stability toward HER, these cocatalyst particles necessitate to be loaded on high surface area and conductive substrates such as carbon nanomaterials (carbon nanotubes,[27] graphene,[28] and MOF derivatives,[29] *etc.*) to ensure high dispersion and structural integrity. Despite proven to be effective, these artificially-synthesized carbon supports are not preferable for large-scale application due to complex synthesis and prohibitive costs.

In this work, we develop a carbon nanosheet-confined Co_2P cocatalyst by a facile *in situ* confinement strategy by embedding ultrahigh-density Co_2P NPs (Co_2P/CPE) within carbonized *Pleurotus eryngii* (CPE). The unique carbon nanosheet framework not only ensures rapid electron transport but also provides abundant anchoring sites for nanoparticle stabilization. When coupled with ErB photosensitizer in a TEOA sacrificial system, the Co_2P/CPE cocatalyst demonstrates remarkable visible-light-driven HER activity (449 µmol h^{-1}, AQE = 8.7% at 500 nm) and unprecedented durability over 36 h continuous operation. Furthermore, the versatility of Co_2P/CPE as a HER

---

[a] School of Chemistry and Chemical Engineering, North Minzu University, Yinchuan, 750021, P. R. China. E-mail: sxmin@nun.edu.cn
[b] Ningxia Key Laboratory of Solar Chemical Conversion Technology, North Minzu University, Yinchuan, 750021, P. R. China
[c] Analysis and Testing Center of Ningxia Hui Autonomous Region, North Minzu University, Yinchuan, 750021, P. R. China

† Electronic supplementary information (ESI) available: Experimental details and additional figures. See DOI: https://doi.org/10.1039/d5ya00112a

cocatalyst is confirmed when combined with CdS NPs under visible light irradiation ($\lambda \geq 420$ nm).

Fig. 1a schematically illustrates the preparation process of the Co_2P/CPE by a facile *in situ* confinement strategy involving successive physical absorption of active species ions within *Pleurotus eryngii* (PE), two-step carbonization, and low-temperature phosphidation (see experimental details in the ESI†). The selection of PE as the carbon precursor is due to its easy availability, low cost, sustainability, and high adsorption/binding capacity towards metal ions,[30] which are beneficial for immobilizing high density metal active species. First, PE was cut into thin slices, washed, and freezing-dried to get rid of all the water in the structure without shrinkage. Then, the dry PE slice was soaked into a $Co(NO_3)_2$ aqueous solution to obtain Co^{2+}-adsorbed PE (Co^{2+}-PE). Then the dry Co^{2+}-PE was carbonized to obtain carbonized PE-supported metallic Co NPs (Co/CPE). Finally, the as-obtained Co/CPE was phosphidated using NaH_2PO_2 to convert embedded Co NPs into Co_2P NPs, eventually obtaining Co_2P/CPE. The scanning electron microscopy (SEM) images of Fig. 1b and c indicated that the Co/CPE possesses thin sheet-like structure and high-density Co NPs with a small size of *ca.* 20 nm are found to be firmly embedded on the surfaces of CPE. After phosphidation, although the sheet-like structure and uniform distribution of the NPs are largely retained in the resulting Co_2P/CPE (Fig. 1d), the size of obtained Co_2P NPs is slightly decreased to *ca.* 15 nm (Fig. 1e), confirming the successful conversion of metallic Co to Co_2P. The reduction in the size of Co_2P NPs is believed to provide more active sites for efficiently catalyzing the photocatalytic HER.[31]

The detailed microstructures of the Co/CPE and Co_2P/CPE was further investigated using the transmission electron microscopy (TEM). As shown in the TEM image of Co/CPE (Fig. 1f), consistent with the SEM results, thin and porous carbon nanosheets were derived from the carbonization of PE. Moreover, a large number of Co NPs with average size of 20 nm are found to be uniformly distributed within the carbon nanosheet frameworks. High-resolution TEM (HRTEM) image (Fig. 1g) further reveals clear lattice fringes with an interspacing of 0.202 nm, corresponding to the (111) plane of metallic Co

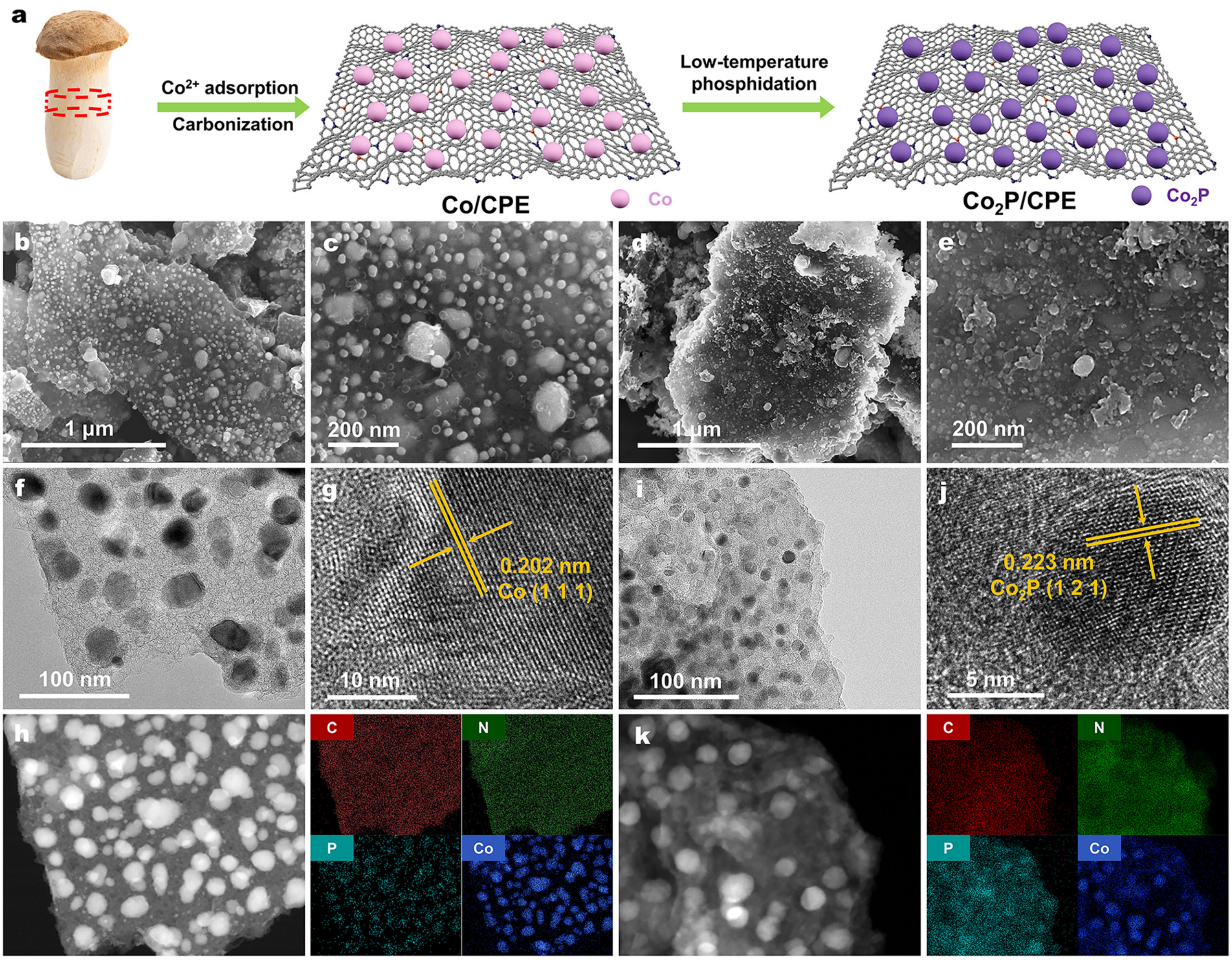

Fig. 1 (a) Schematics of the preparation process of Co_2P/CPE cocatalysts. Low- and high-magnification SEM images of (b) and (c) Co/CPE and (d) and (e) Co_2P/CPE. TEM and HRTEM images (f) and (g) Co/CPE and (i) and (j) Co_2P/CPE. HAADF-STEM images and the corresponding EDX elemental mapping images of (h) Co/CPE and (k) Co_2P/CPE.

phase. Moreover, the high-angle annular dark-field scanning transmission electron microscopy (HAADF-STEM) images of Co/CPE and the corresponding energy dispersive X-ray spectroscopy (EDX) elemental maps (Fig. 1h) further reveal the uniform distribution of Co NPs and the homogenous doping of N and P within the frameworks of carbon nanosheets. As to the Co_2P/CPE, TEM image of Fig. 1i indicates that the carbon nanosheet architectures are well-preserved and the generated Co_2P NPs are still firmly embedded with high dispersion and a reduced size, in good agreement of the SEM results. HRTEM image in Fig. 1j reveals an interspacing of 0.223 nm, which corresponds to lattice plane of (121) of orthorhombic Co_2P phase. Moreover, the HAADF-STEM image of Co_2P/CPE and the corresponding EDX maps (Fig. 1k) clearly demonstrate the perfect overlap of Co and P elements, firming confirming the formation of Co_2P.

The phase structure of the samples was analyzed by using the X-ray diffraction (XRD). As shown in Fig. 2a and Fig. S1a (ESI†), the Co/CPE samples typically exhibit three characteristic diffraction peaks ascribed to metallic Co phase (JCPDS No. 15-0806) at 2θ values of 44.2°, 51.5°, and 78.5°, and the peak intensities of these peaks increase with the increasing concentration of Co solution used in the preparation processes. After low-temperature phosphidation, only the diffraction peaks corresponding to orthorhombic Co_2P (JCPDS No. 32-0306) phase could be observed in all the resulting Co_2P/CPE even at higher Co concentration (Fig. 2a and Fig. S1b, ESI†). Noted that the Bragg peaks of Co_2P phase in Co_2P/CPE samples are more broadened than those of Co phase obtained in corresponding Co/CPE samples, indicating the smaller particle size of Co_2P NPs and/or larger lattice strain due to the strong confinement of carbon nanosheets, consistent with the results of SEM, TEM, and EDX analyses.

The elemental composition and chemical states of Co and P elements in Co/CPE and Co_2P/CPE was then investigated by using the X-ray photoelectron spectroscopy (XPS). The survey XPS spectra (Fig. S2, ESI†) reveal the presence of all the major elements (C, O, Co, and P) in both Co/CPE and Co_2P/CPE, with the P signal in Co_2P/CPE is much stronger than that in Co/CPE. This indicates a successful increase in P species probably due to the formation of Co_2P during phosphidation. In fact, as indicated in Table S1 (ESI†), the P content of Co_2P/CPE (14.19 wt%) determined by inductively coupled plasma optical emission spectroscopy (ICP-OES) is significantly higher than that of Co/CPE (2.54 wt%), with a molar ratio of Co to P of 1.39 : 1 for Co_2P/CPE, confirming the formation of Co_2P by phosphidation. Fig. 2b shows the high-resolution P 2p XPS spectra of Co/CPE and Co_2P/CPE. It is noted that trace amount of P species is also presented in Co/CPE, which may stem from the natural P-containing proteins in the PE. After phosphidation, in addition to the P–O species originating from phosphates due to the inevitable surface air-oxidation, a distinct and strong P–Co peak is observed at 129.6 eV. Furthermore, in the high-resolution XPS spectra of Co 2p (Fig. 2c), it is observed that the Co species in Co/CPE mainly exist in the forms of oxides (Co^{2+} $2p_{3/2}$: 781.4 eV) and metal (Co^0 $2p_{3/2}$: 778.2 eV). After phosphidation, although the Co oxides (Co^{2+} $2p_{3/2}$: 781.8 eV) are still presented in the resulting Co_2P/CPE, their content is significantly reduced while the metallic Co^0 peak completely vanishes. Meanwhile, a new and stronger peak corresponding to Co–P species (778.5 eV) appears in the resulting Co_2P/CPE, confirming the *in situ* confinement of Co_2P within the frameworks of carbon nanosheets. In addition, the N_2 adsorption–desorption measurements (Fig. 2d) indicate that although the specific surface area of Co_2P/CPE (42.6 cm^2 g^{-1}) is slightly lower than that of Co/CPE (54.4 cm^2 g^{-1}), its pore size and volume are increased (Table S1, ESI†), indicating that the phosphidation reaction can partially etch the carbon nanosheet substrate to improve the exposure of the embedded Co_2P NPs and thus can offer more active sites for the photocatalytic HER.

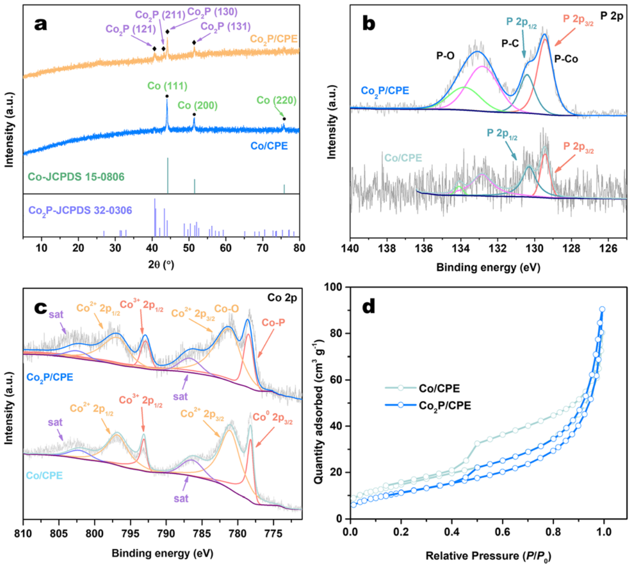

Fig. 2 (a) XRD patterns of Co/CPE and Co_2P/CPE. (b) P 2p and (c) Co 2p XPS spectra of Co/CPE and Co_2P/CPE. (d) N_2 adsorption–desorption isotherms of Co/CPE and Co_2P/CPE.

The cocatalytic activities of Co/CPE and Co_2P/CPE samples towards the photocatalytic HER were investigated in a dye-sensitized system under visible light irradiation ($\lambda \geq 420$ nm) using Erythrosin B (ErB) and triethanolamine (TEOA, pH 8) as the photosensitizer and as the sacrificial reagent, respectively. As shown in Fig. 3a, the HER activities of both Co/CPE and Co_2P/CPE samples are found to gradually increase with increasing Co^{2+} concentration ([Co]) used in the preparation process and reach the highest values as the [Co] equals to 0.2 M. Further increase in the [Co], an obvious decrease in the HER rate is observed for both samples. Clearly, at each [Co], the Co_2P/CPE shows much higher HER activity than Co/CPE, and the highest H_2 evolution rate of Co_2P/CPE is as high as 449 μmol h^{-1}, which is nearly 4 times higher than that of Co/CPE (114 μmol h^{-1}). In addition, the ErB-sensitized Co_2P/CPE exhibits high apparent quantum efficiency (AQE) for the HER under visible light irradiation, and the achievable highest AQE is as high as 8.7% at 500 nm (Fig. 3b). This remarkably enhanced HER activity of Co_2P/CPE could be attributed to the *in situ* confinement of high density Co_2P NSs within carbon

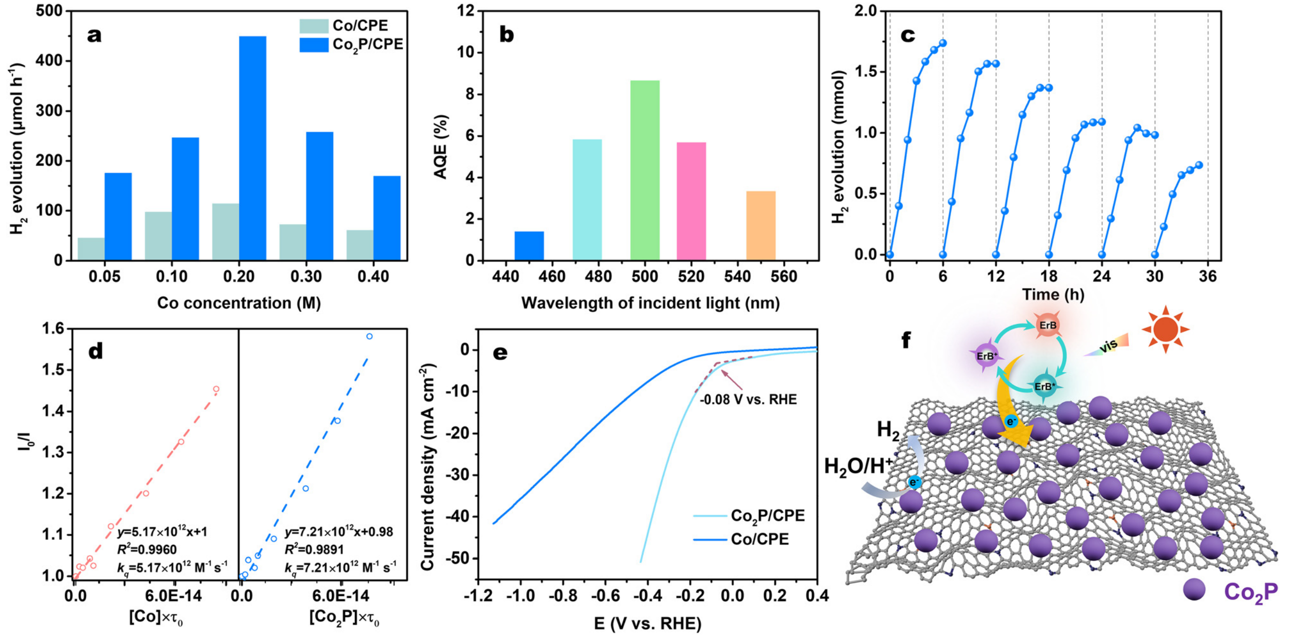

Fig. 3 (a) HER activities of Co/CPE and Co_2P/CPE samples prepared using different concentrations of $Co(NO_3)_2$ in the ErB-TEOA system under visible light irradiation. (b) Dependence of AQE of the HER of ErB-sensitized Co_2P/CPE on the wavelength of incident visible light. (c) HER stability of Co_2P/CPE in the ErB-TEOA system. (d) Stern–Volmer plots for PL emission quenching of ErB solution (10 mM) excited at 480 nm with Co/CPE and Co_2P/CPE (τ_{ErB} = 0.15 ns). (e) HER LSV curves of Co/CPE and Co_2P/CPE. (f) Plausible photocatalytic mechanism of the Co_2P/CPE-catalyzed HER in the ErB-TEOA system under visible light irradiation. Reaction conditions: light source: 30 W white-light LED lamp, $\lambda \geq 420$ nm; TEOA solution, 10 vol%, 100 mL, pH 8; ErB: 0.5 mM; catalyst: 50 mg.

nanosheet substrate, which can provide abundant highly active sites for the HER.

To clarify the important role of the PE-derived carbon nanosheet substrate played in improving the HER activity of embedded Co_2P NPs, the Co_2P NPs without supporting on any substrates were prepared by the direct phosphidation of $Co(NO_3)_2$ using NaH_2PO_2 and tested (see experimental details in the ESI†). The results show that the as-prepared Co_2P NPs are active for the HER in the ErB-TEOA system, but its activity is much lower than that of Co_2P/CPE, probably due to the large particle size (> 100 nm) and thus limited number of active sites (Fig. S3, ESI†). In addition, as evidenced in Fig. S4 (ESI†), the physical mixture of Co_2P NPs and CPE (Co_2P-CPE) is much less active towards the HER than Co_2P/CPE, confirming that the strong coupling interaction between embedded Co_2P PSs and CPE is effective to promoting the electron transfer and thus improving the HER activity. On the other hand, to further highlight the structural superiority of CPE than other biomass-derived carbon supports, a carbonized wood (CW)-supported Co_2P (Co_2P/CW) catalyst was prepared by using the exact same procedure for Co_2P/CPE except using natural wood instead of using PE (see experimental details in the ESI†). Noted that although the as-fabricated Co_2P/CW shows much higher HER activity compared to Co_2P NPs (Fig. S5, ESI†), its activity is still much lower than that of Co_2P/CPE, further confirming the carbon nanosheets derived from PE is favourable for providing large surface area for immobilizing high density Co_2P NPs with small size and high dispersion for efficiently catalyzing the HER.

To further enhance the dye-sensitized HER activity of Co_2P/CPE, the operation parameters of the system including pH value of TEOA solution, concentrations of Co_2P/CPE and photosensitizer, and the type of dye were optimized (Fig. S6, ESI†). At the optimized reaction conditions, the HER stability of Co_2P/CPE in the ErB-TEOA system under visible light irradiation ($\lambda \geq 420$ nm) was evaluated by performing a continuous cycling reaction over a period of 36 h with a cycle every 6 h. At the end of each cycle, the Co_2P/CPE was separated from the reaction solution by centrifugation, washed, and redispersed into the reaction solution containing fresh ErB and TEOA. As demonstrated in Fig. 3c, it is noted that the HER activity of Co_2P/CPE gradually deceases with the reaction cycle, and it still exhibits a high activity even after sixth cycle with an activity retention of more than 44%. The cycled Co_2P/CPE was characterized by using XRD, XPS, and TEM analyses. As indicated in Fig. S7a (ESI†), although no significant change in the phase structure is observed for the cycled Co_2P/CPE, the characteristic peak intensity of Co_2P phase slightly weakens, indicating that the embedded Co_2P NPs would partially detach from the CPE substrate during the centrifugation and washing processes. In addition, the results of XPS analysis indicate that the chemical states of P and Co elements for the cycled Co_2P/CPE does not change significantly (Fig. S7b and c, ESI†). Furthermore, TEM analysis shows that the carbon nanosheet morphology of CPE substrate is well-maintained and high density Co_2P NPs are still well embedded within the matrix of carbon nanosheets with good crystallinity (Fig. S8, ESI†). Therefore, it can be inferred that the observed decrease in the HER activity of Co_2P/CPE during cycling reaction may be due to the partial loss of Co_2P/CPE and the slight detachment of embedded Co_2P NPs.

To get insights into the photoinduced electron transfer process of ErB-sensitized Co_2P/CPE in the reaction system, the photoluminescence (PL) emission quenching behaviours of excited ErB (ErB*) at 480 nm in the presence of TEOA, Co/CPE, and Co_2P/CPE were investigated. As shown in Fig. S9a and b (ESI†), the TEOA can reductively quench the PL emission of ErB* following a linear Stern–Volmer rule with a small rate constant (k_q) of $1.84 \times 10^9\ M^{-1}\ s^{-1}$. On the contrary, both Co/CPE and Co_2P/CPE can efficiently oxidatively quench the PL emission of ErB* (Fig. S9c and d, ESI†) with much higher rate constants of $5.17 \times 10^{12}\ M^{-1}\ s^{-1}$ and $7.21 \times 10^{12}\ M^{-1}\ s^{-1}$ (Fig. 3d) based on the concentrations of embedded Co and Co_2P, respectively, which are three orders of magnitude higher than that of TEOA. The enhanced k_q of Co_2P/CPE compared to Co/CPE suggests a more efficient electron transfer from ErB* to Co_2P/CPE due to the formation of Co_2P NPs. These results suggest that when both TEOA and Co_2P/CPE coexist in the reaction system, photogenerated electrons will be preferentially transferred from ErB* to Co_2P/CPE *via* the oxidative quenching pathway,[32,33] after which ErB^+ can accept electrons from TEOA to regenerate ErB, albeit with that the electron transfer from ErB^- obtained *via* the reductive quenching of ErB* to Co_2P/CPE would not be ruled out. In addition, as shown in Fig. 3e, Co_2P/CPE exhibits a much higher electrocatalytic activity towards the HER compared to Co/CPE. Specifically, the Co_2P/CPE only requires overpotential of 160 mV to achieve a current density of 10 mA cm^{-2}, which is much lower than that of Co/CPE (460 mV). This result strongly suggests that the *in situ* confined Co_2P NPs within carbon nanosheet matrix of CPE are capable of efficiently catalyzing the photocatalytic HER. Based on the above results, a plausible mechanism for the photocatalytic HER is proposed, as shown in Fig. 3f. Upon the visible light irradiation, the ErB molecules are excited to form the ErB*. Because the estimated reduction potential of ErB is −0.91 V *vs.* NHE,[34] which is more negative than the reduction potential of Co_2P (−0.69 V *vs.* NHE) (−0.08 V *vs.* RHE as indicated in Fig. 3e)

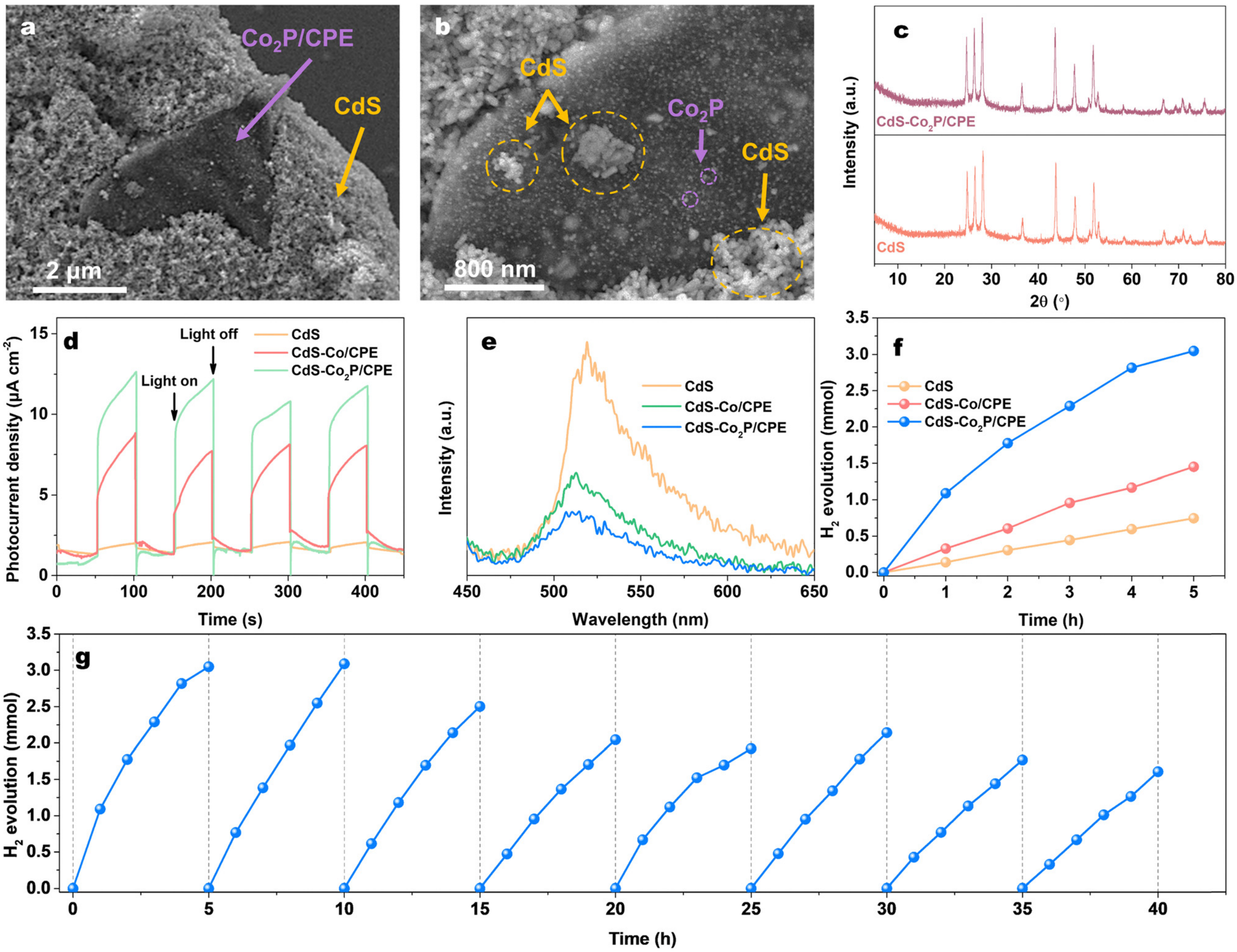

Fig. 4 (a) Low- and (b) high-magnification SEM images of CdS–Co_2P/CPE. (c) XRD patterns of pristine CdS and CdS–Co_2P/CPE. (d) Photocurrent responses of pristine CdS, CdS–Co/CPE, and CdS–Co_2P/CPE. (e) PL spectra of pristine CdS, CdS–Co/CPE, and CdS–Co_2P/CPE (Excitation wavelength: 370 nm). (f) Time courses of photocatalytic H_2 evolution of CdS, CdS–Co/CPE and CdS–Co_2P/CPE. (g) Cycling stability of CdS–Co_2P/CPE. Reaction conditions: light source: 300 W Xe lamp, $\lambda \geq 420$ nm; LA solution, 10 vol%, 100 mL; catalyst: 100 mg.

in the Co_2P/CPE, the excited ErB* will be oxidatively quenched *via* the direct electron transfer to carbon nanosheet and then to embedded Co_2P NPs. Due to the strong coupling of Co_2P NPs with underlying CPE substrate, the photoinduced electron transfer will be greatly promoted to high density embedded Co_2P NPs, where the H_2O is efficiently reduced to produce H_2 gas, while the oxidative ErB cation radicals are reduced back to ground-state ErB by TEOA, thus completing the catalytic cycles.

In order to confirm the generality of Co_2P/CPE as the cocatalyst for photocatalytic HER, a semiconductor-based composite photocatalyst (CdS–Co_2P/CPE) was prepared by simply mixing Co_2P/CPE (5 mg) with visible-light-responsive CdS (100 mg) and tested for the photocatalytic HER under visible light irradiation ($\lambda \geq 420$ nm) (see experimental details in the ESI†). For a comparison, the composite of Co/CPE and CdS was also prepared (CdS–Co/CPE). The SEM images of CdS–Co_2P/CPE (Fig. 4a and b) shows that the CdS NPs are heavily coated on the surfaces of carbon nanosheet matrix of Co_2P/CPE cocatalyst, which would ensure an intimate contact for fast interfacial electron transfer. The XRD patterns of pristine CdS and CdS–Co_2P/CPE are shown in Fig. 4c. The results indicate that the physical mixing does not change the phase structure of both CdS and Co_2P/CPE in the CdS–Co_2P/CPE, which are favourable for CdS and Co_2P/CPE being used as the light harvester and HER cocatalyst, respectively. As a result, the integration of Co_2P/CPE with CdS is found to be remarkably enhance the photocurrent response of the resulting (see experimental details in the ESI†) CdS–Co_2P/CPE (Fig. 4d) under visible light irradiation, which is also much higher than that of CdS–Co/CPE, suggesting that the Co_2P/CPE as the cocatalyst is more effective to greatly promoting the charge separation and transfer of CdS than Co/CPE. In parallel, the PL measurements (Fig. 4e) (see experimental details in the ESI†) further demonstrate that strong PL emission of CdS at 520 nm excited at 370 nm originating from significant charge recombination can be greatly quenched by Co_2P/CPE with a quenching efficiency higher than that with Co/CPE, further confirming efficient electron transfer from CdS to Co_2P/CPE for improving the charge separation.[35,36]

Afterwards, the photocatalytic HER activities of the pristine CdS, CdS–Co/CPE, and CdS–Co_2P/CPE were evaluated by using the lactic acid as the sacrificial reagent under visible light irradiation ($\lambda \geq 420$ nm). As indicated in Fig. 4f, the pristine CdS exhibits low photocatalytic HER activity (746 μmol in 5 h) owing to the fast charge recombination as expected. After being integrated with Co/CPE, although the resulting CdS–Co/CPE shows an enhanced HER activity (703 μmol in 5 h) compared to pristine CdS, but the enhancement factor is low due to the low activity of Co/CPE cocatalyst. In strong contrast, the CdS–Co_2P/CPE demonstrates exceptionally high HER activity, producing 3049 μmol of H_2 in 5 h, which is 4 and 2 times higher than those of pristine CdS and CdS–Co/CPE, respectively. In addition, it is clear that although the HER activity of Co_2P/CPE is lower than those of metal phosphide cocatalysts prepared from expensive precursors (Table S2, ESI†), the high cost-effectiveness of Co_2P/CPE is still beneficial for its large-scale practical application. More importantly, besides its high cocatalytic HER activity, the Co_2P/CPE also exhibits good stability in catalyzing H_2 evolution when combined with CdS, as shown in Fig. 4g. Even after a 40 h of cyclic stability testing, the cycled CdS–Co_2P/CPE is still highly active towards the HER with an activity retention of 52%. The XRD and SEM characterizations (Fig. S10, ESI†) of cycled CdS–Co_2P/CPE indicate no significant changes in phase structure and morphology, suggesting the slight decrease in the HER activity would be most likely due to the inevitable photocorrosion of CdS rather than the deactivation of Co_2P/CPE cocatalyst. These results further confirm the high versatility of Co_2P/CPE as a highly active and stable cocatalyst for promoting the photocatalytic HER activity.

In summary, we have successfully fabricated an efficient and cost-effective carbon-based cocatalyst (Co_2P/CPE) through the *in situ* confinement of ultrahigh-density Co_2P nanoparticles within carbon nanosheet matrix of carbonized *Pleurotus eryngii*. The synergistic architecture of ultrathin carbon nanosheets and maximized exposure of Co_2P active sites confers exceptional cocatalytic performance in the ErB-TEOA photocatalytic system, delivering a remarkable H_2 evolution rate of 449 μmol h^{-1} under visible light with an AQE of 8.7% at 500 nm. The structural integrity of Co_2P/CPE ensures remarkable stability over a prolonged HER without significant performance degradation. Furthermore, Co_2P/CPE cocatalyst demonstrates universal enhancement ability to significantly boost the photocatalytic HER activity of CdS by visible light. This work establishes a paradigm for designing sustainable and high-performance HER cocatalysts through the rational integration of biomass-derived carbon architectures with precisely engineered active sites.

Conflicts of interest

There are no conflicts to declare.

Data availability

The data supporting this article have been included as part of the ESI.†

Acknowledgements

This work was financially supported by the National Natural Science Foundation of China (22162001 and 62364001) and the Ningxia Autonomous Region Key Research Plan of Special Talent Introduction (2024BEH04081). We also highly appreciated Mr Yongxin Sun, Miss Chun Hu, Miss Kaige Xu, and Miss Yuyu Wang at Analysis and Testing Center of North Minzu University for their assistance with SEM, XRD, ICP-OES, and XPS analyses.

References

1 H. Stančin, H. Mikulčić, X. Wang and N. Duić, *Renewable Sustainable Energy Rev.*, 2020, **128**, 109927.
2 A. Hasani, M. Tekalgne, Q. V. Le, H. W. Jang and S. Y. Kim, *J. Mater. Chem. A*, 2019, **7**, 430–454.

3 T. Takata, J. Z. Jiang, Y. Sakata, M. Nakabayashi, N. Shibata, V. Nandal, K. Seki, T. Hisatomi and K. Domen, *Nature*, 2020, **581**, 411–414.

4 M. Sayed, J. Yu, G. Liu and M. Jaroniec, *Chem. Rev.*, 2022, **122**, 10484–10537.

5 Z. Liang, R. Shen, Y. H. Ng, P. Zhang, Q. Xiang and X. Li, *J. Mater. Sci. Technol.*, 2020, **56**, 89–121.

6 S. Sharma and S. K. Ghoshal, *Renewable Sustainable Energy Rev.*, 2015, **43**, 1151–1158.

7 C. Gunathilake, I. Soliman, D. Panthi, P. Tandler, O. Fatani, N. A. Ghulamullah, D. Marasinghe, M. Farhath, T. Madhujith, K. Conrad, Y. H. Du and M. Jaroniec, *Chem. Soc. Rev.*, 2024, **53**, 10900–10969.

8 J. Pan, G. Zhang, Z. Guan, Q. Zhao, G. Li, J. Yang, Q. Li and Z. Zou, *J. Energy Chem.*, 2021, **58**, 408–414.

9 L. F. Hong, R. T. Guo, Y. Yuan, X. Y. Ji, Z. D. Lin, Z. S. Li and W. G. Pan, *ChemSusChem*, 2020, **14**, 539–557.

10 R. Z. Li, J. D. Luan, Y. Zhang, L. D. Jiang, H. B. Yan, Q. Y. Chi and Z. Yan, *Renewable Sustainable Energy Rev.*, 2024, **206**, 114863.

11 X. Y. Xu, L. Shi, S. Zhang, Z. M. Ao, J. Q. Zhang, S. B. Wang and H. Q. Sun, *Chem. Eng. J.*, 2023, **469**, 143972.

12 P. Priyadharsini, P. SundarRajan, K. G. Pavithra, S. Naveen, S. SanjayKumar, D. Gnanaprakash, J. Arun and A. Pugazhendhi, *J. Clean. Prod.*, 2023, **426**, 139180.

13 Y.-H. Chung, K. Han, C.-Y. Lin, D. O'Neill, G. Mul, B. Mei and C.-M. Yang, *Catal. Today*, 2020, **356**, 95–100.

14 W. Raza, K. Ahmad, R. A. Khan and H. Kim, *Int. J. Hydrogen Energy*, 2023, **48**, 29071–29081.

15 Z. H. Xu, W. H. Yue, C. C. Li, L. Z. Wang, Y. K. Xu, Z. W. Ye and J. L. Zhang, *ACS Nano*, 2023, **17**, 11655–11664.

16 Z. Y. Ma, X. J. Kuang, S. Q. Peng and Y. X. Li, *Adv. Funct. Mater.*, 2025, 2425117.

17 X. M. Chen and Y. X. Li, *Small Methods*, 2025, **9**, 2401075.

18 J. X. Zhang, W. F. Yao, C. P. Huang, P. H. Shi and Q. J. Xu, *J. Mater. Chem. A*, 2017, **5**, 12513–12519.

19 J. Ge, W. Zhang, J. Tu, T. Xia, S. Chen and G. Xie, *Small*, 2020, **16**, 2001856.

20 H. M. Zhou, R. L. Chen, C. C. Han, P. Wang, Z. F. Tong, B. H. Tan, Y. Z. Huang and Z. F. Liu, *J. Colloid Interface Sci.*, 2022, **610**, 126–135.

21 X. Z. Yue, S. S. Yi, R. W. Wang, Z. T. Zhang and S. L. Qiu, *Small*, 2017, **13**, 1603301.

22 Z. C. Sun, M. S. Zhu, X. S. Lv, Y. Y. Liu, C. Shi, Y. Dai, A. J. Wang and T. Majima, *Appl. Catal., B*, 2019, **246**, 330–336.

23 A. Kumar, P. Shandilya, D. N. Vo, G. Sharma, M. Naushad, P. Dhiman and F. J. Stadler, *Environ. Chem. Lett.*, 2022, **20**, 597–632.

24 C. Cai, Y. Teng, J. H. Wu, J. Y. Li, H. Y. Chen, J. H. Chen and D. B. Kuang, *Adv. Funct. Mater.*, 2020, **30**, 2001478.

25 Q. Q. Sun, Z. B. Yu, R. H. Jiang, Y. P. Hou, L. Sun, L. Qian, F. Y. Li, M. J. Li, Q. Ran and H. Q. Zhang, *Nanoscale*, 2020, **12**, 19203–19212.

26 Y. Yang, W. Ren, Y. Y. Liu, C. Cai, X. Zheng, S. G. Meng and L. W. Zhang, *J. Colloid Interface Sci.*, 2023, **649**, 547–558.

27 Z. Mou, T. T. Meng, J. C. Li, Y. H. Wang, X. P. Wang, H. Y. Guo, W. Meng and K. J. Zhang, *Int. J. Hydrogen Energy*, 2024, **51**, 748–757.

28 L. J. Fang, X. L. Wang, Y. H. Li, P. F. Liu, Y. L. Wang, H. D. Zeng and H. G. Yang, *Appl. Catal., B*, 2017, **200**, 578–584.

29 C. X. Chen, Y. Y. Xiong, X. Zhong, P. C. Lan, Z. W. Wei, H. J. Pan, P. Y. Su, Y. J. Song, Y. F. Chen, A. Nafady Sirajuddi and S. Q. Ma, *Angew. Chem., Int. Ed.*, 2022, **61**, e202114071.

30 X. X. Ji, Y. Liu, Z. H. Ma, Y. Han, X. Wang and G. W. Sun, *Diamond Relat. Mater.*, 2024, **148**, 111429.

31 D. F. Sun, J. X. Liu, P. P. Qiang, W. Q. Ma, Y. N. Qu, S. K. Ding, Y. Yuan, Z. R. Li and B. S. Xu, *Electrochim. Acta*, 2025, **521**, 145915.

32 L. Wang, H. H. Wu, Y. F. Lin, M. Y. Wang, Z. L. Wang, W. D. Xing, S. B. Wang and Y. X. Fang, *ChemSusChem*, 2025, 2500338.

33 B. F. Li, W. J. Wang, J. W. Zhao, Z. Y. Wang, B. Su, Y. D. Hou, Z. X. Ding, W. J. Ong and S. B. Wang, *J. Mater. Chem. A*, 2021, **9**, 10270–10276.

34 J. Y. Xu, Y. X. Li and S. Q. Peng, *Int. J. Hydrogen Energy*, 2015, **40**, 353–362.

35 D. D. Zheng, L. L. Yang, W. W. Chen, Y. X. Fang and X. C. Wang, *ChemSusChem*, 2021, **14**, 3821–3824.

36 B. Su, M. Zheng, W. Lin, X. F. Lu, D. Y. Luan, S. B. Wang and X. W. Lou, *Adv. Energy Mater.*, 2023, **13**, 2203290.